Pramana – J. Phys. (2022) 96:25
https://doi.org/10.1007/s12043-021-02268-w

Random transverse single-ion anisotropies in the mixed spin-1 and spin-1/2 Blume–Capel quantum model: Mean-field theory calculations

G SETO[1], R A A YESSOUFOU[1,2], A KPADONOU[3] and E ALBAYRAK[4],*

[1]Institute of Mathematic and Physical Sciences (IMSP), Dangbo, Republic of Benin
[2]Department of Physics, University of Abomey-Calavi, Godomey, Republic of Benin
[3]ENS and Laboratory of Physics and Applications (LPA), d'Abomey, Benin
[4]Department of Physics, Erciyes University, 38039 Kayseri, Turkey
*Corresponding author. E-mail: albayrak@erciyes.edu.tr

MS received 8 June 2021; revised 20 August 2021; accepted 14 September 2021

Abstract. We have used mean-field theory based on the Bogoliubov inequality for the free energy to study the effects of random transverse single-ion anisotropies and magnetic field on the mixed spin-1 and spin-1/2 Blume–Capel quantum model with the coordination number $z = 3$. The interactions of the transverse crystal fields D_x and D_y act only on the spin-1 sites and are randomly active with probability p and q and inactive with probability $1-p$ and $1-q$ respectively. The thermal behaviours of the order parameters are studied to determine the nature of phase transitions and to calculate the phase diagrams on the $(\varphi_x = D_x/Jz, k_{\mathrm{B}}T/J)$, $(p, k_{\mathrm{B}}T/J)$ and $(q, k_{\mathrm{B}}T/J)$ planes. It is found that the model exhibits only second-order phase transitions. The compensation temperatures are also observed and their lines, T_{comp}-lines, are depicted on the $(\varphi_x, k_{\mathrm{B}}T/J)$ planes. The hysteresis loops are obtained by introducing an external magnetic field on the system which reveals that the coercive field decreases with temperature and with positive values of φ_x and φ_y. It is also found that remanent magnetisation increases with negative values of φ_x and φ_y.

Keywords. Blume–Capel quantum model; mixed spin-1 and spin-1/2; random transverse crystal field; compensation temperature; hysteresis loops.

PACS Nos **61.10.Nz; 61.66.Fn; 75.40.Gb**

1. Introduction

Widely studied for the additional properties they exhibit compared to those of the single-spin systems, the mixed-spin systems provide fertile ground for scientific investigations. Several experimental works have shown that the molecue-based magnetic materials can be described by mixed-spin systems [1–4]. The possibility for these systems to yield compensation behaviours gives to magnetic materials very important properties used in many technological applications such as: the thermomagnetic recording and magneto-optical readout applications, microwave communication systems, electric power transformers and dynamo and high-fidelity speakers [5–9]. For a better knowledge of the properties of these systems, it is important to model them theoretically and to simulate them. Thus, several physical models are proposed. The Blume–Capel model [10,11] is one such model which takes into account the effects of the crystal field in the systems. This model is therefore used to study a large number of mixed spin systems using different techniques.

Many studies concerning the mixed spin-1 and spin-1/2 system have been reported in the literature. In most of these systems, the longitudinal component of crystal field (LCF) alone has been considered in the Hamiltonian. Later, many other studies revealed that the transverse component of crystal field (TCF) also affects the critical behaviours of the mixed spin systems. Among these, we can cite: the critical behaviours of a mixed spin-1/2 and spin-s_B Ising system with TCF [12], the study on simple cubic lattice of the bond-diluted mixed spin-1/2 and spin-1 Ising model with uniaxial and biaxial single-ion anisotropies [13], the study of ferrimagnetic multilayer system which constitutes L layers of spin-$1/2$ atoms, L layers of spin-1 atoms and a disordered interface between them [14], the critical properties of a ferromagnetic (FM) or ferrimagnetic mixed Ising bilayer system with both spin-$1/2$ and spin-1 (or spin-$3/2$) in a TCF [15], the TCF effects on FM or ferrimagnetic bilayer system with different spins ($S_A = 1/2$ and $S_B = 1, 3/2$) [16], the study of critical properties of the mixed spin-$1/2$ and spin-1 Ising model with bond dilution or bond percolation threshold within TCF and bimodal magnetic field [17], the compensation properties of mixed spin-$1/2$ and spin-1 Ising model with a TCF and external magnetic field [18] and the mixed spin-$1/2$ and spin-1 Ising chain with LCF and TCF solved by using the Jordan–Wigner transformation [19].

It is important to specify that the presence of TCF or biaxial-ion anisotropy term, which brings into play the x and y components of the spin operators is at the base of the difficulties encountered during the resolution of the Ising models containing these terms. Indeed, these spin operators do not commute with each other, leading to quantum fluctuations in the system. Thus, the spin systems are quantum mechanical and will be studied in quantum models such as the Heisenberg or Blume–Capel quantum (BCQ) models. Some works using various calculation techniques have been carried out on the mixed spin-$1/2$ and spin-1 system. For example, the geometry frustration of the mixed spin-$1/2$ spin-S Ising–Heisenberg system was studied by using Kambe projection method, decoration–iteration transformation and transfer-matrix method [20]. The mixed spin-$1/2$ and spin-1 system with a biaxial single-ion anisotropy term has been solved exactly on honeycomb and diced lattices [21–23]. They have been also studied within the conventional effective field theory based on differential operator with probability distribution [13,16,24]. Recently, the effects of TCF in mixed spin-$1/2$ and spin-1 Ising Heisenberg model on honeycomb lattice was examined using mean-field approximation [25].

It should be noted that none of these works have focussed solely on the effects of two TCFs, D_x and D_y. In the literature, studies integrating the effects of TCF, D_x and D_y, have only been carried out for spin-1 and spin-$3/2$ in the BCQ model using the mean-field theory based on the Bogoliubov inequality for the Gibbs free energy [26,27]. In order to extend the calculations carried out in these last two works to a mixed spin system, we have introduced the direct product technique to study the effects of random transverse single-ion anisotropies (RTSIA) in the mixed spin-1 and spin-$1/2$ Blume–Capel quantum model to which this work has been devoted.

This work is organised as follows: In §2, we describe the Blume–Capel quantum model for the mixed spin-(1, $1/2$) under two random transverse single-ion anisotropies by using the mean-field theory based on the Bogoliubov inequality for the free energy. In §3, results and discussion are given. Section 4 is devoted to the conclusions.

2. Model and formalism

In order to investigate the effects of RTSIA on the magnetic properties of the mixed spin-(1, $1/2$) BCQ model, we first give the Hamiltonian as

$$\hat{H} = -J \sum_{<i,j>} \hat{S}^z_{iA}\hat{S}^z_{jB} + \sum_i D_{iA}(\hat{S}^z_{iA})^2 + \sum_i D'_{iA}(\hat{S}^x_{iA})^2 - h\Big(\sum_i \hat{S}^z_{iA} + \sum_j \hat{S}^z_{jB}\Big), \quad (1)$$

where $\hat{S}^\delta_{iA}$ and $\hat{S}^\delta_{jB}$ with $\delta = x, z$ are the components of spin-1 and spin-$1/2$ operators for the sublattices A and B, respectively. $J > 0$ is the ferromagnetic exchange interaction between the nearest-neighbour (NN) S_{iA} and S_{jB}. D_{iA} and D'_{iA} are the random LCF and TCF parameters acting only on sites with spin-1. h is the longitudinal external magnetic field acting on spins of sublattices A and B. Starting from spin identity $S_A(S_A+1) = (S^x_A)^2 + (S^y_A)^2 + (S^z_A)^2$ and assuming that $D_{iA} - D'_{iA} = D^x_{iA}$ and $D_{iA} = D^y_{iA}$ [26], the Hamiltonian of eq. (1) becomes

$$\hat{H} = -J \sum_{\langle i,j \rangle} \hat{S}^z_{iA}\hat{S}^z_{jB} - \sum_i D^x_{iA}(\hat{S}^x_{iA})^2 - \sum_i D^y_{iA}(\hat{S}^y_{iA})^2 - h\Big(\sum_i \hat{S}^z_{iA} + \sum_j \hat{S}^z_{jB}\Big). \quad (2)$$

This new form of the Hamiltonian gives a good account of certain experimental results carried out on multilayer sandwich films [28–31].

To study this model, we shall resort to the mean-field theory based on Bogoliubov inequality for the Gibbs free energy given by

$$F \le F_0 + \langle \hat{H} - \hat{H}_0 \rangle_0 \equiv \Phi(\eta_A, \eta_B), \quad (3)$$

where F is the exact free energy of the model described by the Hamiltonian given in eq. (2). F_0 is the free energy of the trial Hamiltonian $\hat{H}_0$ which depends on variational parameters η_A and η_B. $\langle \hat{H} - \hat{H}_0 \rangle_0$ is the thermal average of $(\hat{H} - \hat{H}_0)$ over the ensemble defined by the trial Hamiltonian $\hat{H}_0$. For our calculations, $\hat{H}_0$ is given by

$$\hat{H}_0 = -\eta_A \sum_i \hat{S}^z_{iA} - \eta_B \sum_j \hat{S}^z_{jB}$$

$$
\begin{aligned}
&-\sum_i D^x_{iA}(\hat{S}^x_{iA})^2-\sum_i D^y_{iA}(\hat{S}^y_{iA})^2\\
&-h(\sum_i \hat{S}^z_{iA}+\sum_j \hat{S}^z_{jB}).
\end{aligned}
\tag{4}
$$

Using the same approach as in [25], one can rewrite $\hat{H}_0$ as

$$
\hat{H}_0=\sum_{i,j}-\hat{H}_0^{(ij)},
\tag{5}
$$

where

$$
\begin{aligned}
-\hat{H}_0^{(ij)}&=\eta_A\hat{S}^z_{iA}+\eta_B\hat{S}^z_{jB}+D^x_{iA}(\hat{S}^x_{iA})^2+D^y_{iA}(\hat{S}^y_{iA})^2\\
&\quad+h(\hat{S}^z_{iA}+\hat{S}^z_{jB}).
\end{aligned}
\tag{6}
$$

The components of spin-1 and spin-1/2 operators involved are defined as follows:

$$
\hat{S}^x_{iA}=\frac{1}{\sqrt{2}}\begin{pmatrix}0&1&0\\1&0&1\\0&1&0\end{pmatrix},
$$

$$
\hat{S}^y_{iA}=\frac{1}{\sqrt{2}}\begin{pmatrix}0&-i&0\\i&0&-i\\0&i&0\end{pmatrix}\text{ where }\ i^2=-1
$$

$$
\hat{S}^z_{iA}=\begin{pmatrix}1&0&0\\0&0&0\\0&0&-1\end{pmatrix},\ \hat{S}^z_{jB}=\frac{1}{2}\begin{pmatrix}1&0\\0&-1\end{pmatrix}.
$$

Since the basis vectors of spin-1 and spin-1/2 are defined in spaces of dimensions 3 and 2 respectively, the space of dimension 6 is suitable for carrying out the study of the mixed spin-1 and spin-1/2 systems. Thus, we shall use direct products with unitary matrix $I_{2\times2}$ and $I_{3\times3}$ which are written as

$$
I_{2\times2}=\begin{pmatrix}1&0\\0&1\end{pmatrix},\ I_{3\times3}=\begin{pmatrix}1&0&0\\0&1&0\\0&0&1\end{pmatrix}.
$$

In these conditions, $\hat{H}_0^{(ij)}$ becomes

$$
\begin{aligned}
-\hat{H}_0^{(ij)}&=(\eta_A+h)\hat{S}^z_{iA}\otimes I_{2\times2}+(\eta_B+h)I_{3\times3}\otimes\hat{S}^z_{jB}\\
&\quad+D^x_{iA}(\hat{S}^x_{iA})^2\otimes I_{2\times2}+D^y_{iA}(\hat{S}^y_{iA})^2\otimes I_{2\times2}.
\end{aligned}
\tag{7}
$$

From eq. (7), we obtain the matrix 6 × 6 representing the operator $-\hat{H}_0^{(ij)}$ as

$$
-\hat{H}_0^{(ij)}=\begin{pmatrix}
a_{11}&0&0&0&\Delta_i&0\\
0&a_{22}&0&0&0&\Delta_i\\
0&0&a_{33}&0&0&0\\
0&0&0&a_{44}&0&0\\
\Delta_i&0&0&0&a_{55}&0\\
0&\Delta_i&0&0&0&a_{66}
\end{pmatrix},
$$

where

$$
\begin{aligned}
a_{11}&=\eta_A+\frac{\eta_B}{2}+\delta_i+\frac{3h}{2},\\
a_{22}&=\eta_A-\frac{\eta_B}{2}+\delta_i+\frac{h}{2},\\
a_{33}&=\frac{\eta_B}{2}+2\delta_i+\frac{h}{2},\\
a_{44}&=-\frac{\eta_B}{2}+2\delta_i-\frac{h}{2},\\
a_{55}&=-\eta_A+\frac{\eta_B}{2}+\delta_i-\frac{h}{2},\\
a_{66}&=-\eta_A-\frac{\eta_B}{2}+\delta_i-\frac{3h}{2},\\
\Delta_i&=\frac{D^x_{iA}-D^y_{iA}}{2},\ \delta_i=\frac{D^x_{iA}+D^y_{iA}}{2}.
\end{aligned}
$$

The eigenvalues of the operator $-\hat{H}_0^{(ij)}$ are calculated as

$$
\begin{aligned}
\lambda_{1,2}&=\frac{1}{2}\left[4\delta_i\pm(h+\eta_B)\right],\\
\lambda_{3,4}&=\frac{1}{2}[2\delta_i-\eta_B-h\pm2\sqrt{(\eta_A+h)^2+\Delta_i^2}],\\
\lambda_{5,6}&=\frac{1}{2}[2\delta_i+\eta_B+h\pm2\sqrt{(\eta_A+h)^2+\Delta_i^2}].
\end{aligned}
\tag{8}
$$

By exploiting eq. (8), one gets Z_0 by using the formula

$$
Z_0=Tr_{ij}[\exp(-\beta\hat{H}_0^{(ij)})]=\sum_{l=1}^{6}\exp^{(\beta\lambda_l)},
\tag{9}
$$

where λ_l represents the eigenvalues of the operator $-\hat{H}_0^{(ij)}$. Thus, the explicit form of the trial partition function Z_0 is calculated as

$$
\begin{aligned}
Z_0&=2\exp(2\beta\delta_i)\cosh\left(\beta\frac{\eta_B+h}{2}\right)\\
&\quad+2\exp\left(\beta\frac{2\delta_i-\eta_B-h}{2}\right)\cosh\left(\beta\sqrt{(\eta_A+h)^2+\Delta_i^2}\right)\\
&\quad+2\exp\left(\beta\frac{2\delta_i+\eta_B+h}{2}\right)\cosh\left(\beta\sqrt{(\eta_A+h)^2+\Delta_i^2}\right).
\end{aligned}
\tag{10}
$$

From eq. (3), one deduces explicitly the free energy per site as

$$
\begin{aligned}
\Phi(\eta_A,\eta_B)&=-k_{\mathrm{B}}T\ln\Bigg[2\exp(2\beta\delta_i)\cosh\left(\beta\frac{\eta_B+h}{2}\right)\\
&\quad+2\exp\left(\beta\frac{2\delta_i-\eta_B-h}{2}\right)\cosh\left(\beta\sqrt{(\eta_A+h)^2+\Delta_i^2}\right)\\
&\quad+2\exp\left(\beta\frac{2\delta_i+\eta_B+h}{2}\right)\cosh\left(\beta\sqrt{(\eta_A+h)^2+\Delta_i^2}\right)\Bigg]\\
&\quad+1/2M_A\eta_A+1/2M_B\eta_B-1/2JzM_AM_B.
\end{aligned}
\tag{11}
$$

Minimising eq. (11) with respect to magnetisations M_A and M_B of sublattices A and B respectively, we obtain the variational parameters $\eta_A = JzM_B$ and $\eta_B = JzM_A$. Thus, the Landau free energy $\Psi = -\beta\Phi$ is given by

$$\begin{aligned}\Psi(M_A, M_B) &= -\frac{M_A M_B}{2\tau}\\ &+ \ln\Bigg[2\exp\left(\frac{\varphi_{ix}+\varphi_{iy}}{2\tau}\right)\cosh\left(\frac{M_A+\varphi_h}{2\tau}\right)\\ &+2\cosh\left(\frac{\sqrt{4(M_B+\varphi_h)^2+(\varphi_{ix}-\varphi_{iy})^2}}{2\tau}\right)\\ &\times\left(\exp\left(\frac{\varphi_{ix}+\varphi_{iy}-\varphi_h-M_A}{2\tau}\right)\right.\\ &\left.+\exp\left(\frac{\varphi_{ix}+\varphi_{iy}+\varphi_h+M_A}{2\tau}\right)\right)\Bigg].\end{aligned} \tag{12}$$

The dimensionless parameters introduced in eq. (12) are defined as follows:

$$\varphi_{ix} = \frac{D^x_{iA}}{Jz}, \quad \varphi_{iy} = \frac{D^y_{iA}}{Jz},$$
$$\varphi_h = \frac{h}{Jz} \quad \text{and} \quad \tau = \frac{1}{\beta Jz}.$$

Using eq. (12), we obtain the explicit forms of sublattices A and B magnetisations which are given by

$$\begin{aligned}M_A = \frac{1}{E}\Bigg[&\frac{4(M_B+\varphi_h)}{\sqrt{4(M_B+\varphi_h)^2+(\varphi_{ix}-\varphi_{iy})^2}}\\ &\times\sinh\left(\frac{\sqrt{4(M_B+\varphi_h)^2+(\varphi_{ix}-\varphi_{iy})^2}}{2\tau}\right)\\ &\times\left(\exp\left(\frac{\varphi_{ix}+\varphi_{iy}-\varphi_h-M_A}{2\tau}\right)\right.\\ &\left.+\exp\left(\frac{\varphi_{ix}+\varphi_{iy}+\varphi_h+M_A}{2\tau}\right)\right)\Bigg]\end{aligned} \tag{13}$$

and

$$\begin{aligned}M_B = \frac{1}{E}\Bigg[&\exp\left(\frac{\varphi_{ix}+\varphi_{iy}}{2\tau}\right)\sinh\left(\frac{M_A+\varphi_h}{2\tau}\right)\\ &+2\cosh\left(\frac{\sqrt{4(M_B+\varphi_h)^2+(\varphi_{ix}-\varphi_{iy})^2}}{2\tau}\right)\\ &\times\left(\exp\left(\frac{\varphi_{ix}+\varphi_{iy}+\varphi_h+M_A}{2\tau}\right)\right.\\ &\left.-\exp\left(\frac{\varphi_{ix}+\varphi_{iy}-\varphi_h-M_A}{2\tau}\right)\right)\Bigg],\end{aligned} \tag{14}$$

where

$$\begin{aligned}E &= \exp\left(\frac{\varphi_{ix}+\varphi_{iy}}{2\tau}\right)\cosh\left(\frac{M_A+\varphi_h}{2\tau}\right)\\ &+\cosh\left(\frac{\sqrt{4(M_B+\varphi_h)^2+(\varphi_{ix}-\varphi_{iy})^2}}{2\tau}\right)\\ &\times\left(\exp\left(\frac{\varphi_{ix}+\varphi_{iy}-\varphi_h-M_A}{2\tau}\right)\right.\\ &\left.+\exp\left(\frac{\varphi_{ix}+\varphi_{iy}+\varphi_h+M_A}{2\tau}\right)\right).\end{aligned} \tag{15}$$

The RTSIA are governed by the bimodal distributions given by

$$\begin{aligned}P(\varphi_{ix}) &= p\delta(\varphi_{ix}-\varphi_x)+(1-p)\delta(\varphi_{ix}),\\ P(\varphi_{iy}) &= q\delta(\varphi_{iy}-\varphi_y)+(1-q)\delta(\varphi_{iy}).\end{aligned} \tag{16}$$

Under these distributions, while one part of sites with spin-1 is under the effects of RTSIA with the probabilities p and q respectively, the other part is not subject to any influence of RTSIA. This means that the total number of sites of sublattice A is N_A. D_x and D_y act respectively on a part of N_A with the probability p and q. The other part of N_A is not under the influence of the crystal field. The effects of randomness is given by the average over the disorders. Then we shall calculate the average magnetisations for the two sublattices using the following formula:

$$\langle M_A\rangle_c = \int\int M_A P(\varphi_{ix})P(\varphi_{iy})\mathrm{d}\varphi_{ix}\mathrm{d}\varphi_{iy} \tag{17}$$

and

$$\langle M_B\rangle_c = \int\int M_B P(\varphi_{ix})P(\varphi_{iy})\mathrm{d}\varphi_{ix}\mathrm{d}\varphi_{iy}. \tag{18}$$

Assuming that $M_A = M_A(\varphi_{ix}, \varphi_{iy})$ and $M_B = M_B(\varphi_{ix}, \varphi_{iy})$, one obtains the complete expressions of sublattice magnetisations as

$$\begin{aligned}\langle M_A\rangle_c &= pqM_A(\varphi_x,\varphi_y)+p(1-q)M_A(\varphi_x,0)\\ &\quad+q(1-p)M_A(0,\varphi_y)\\ &\quad+(1-p)(1-q)M_A(0,0),\\ \langle M_B\rangle_c &= pqM_B(\varphi_x,\varphi_y)+p(1-q)M_B(\varphi_x,0)\\ &\quad+q(1-p)M_B(0,\varphi_y)\\ &\quad+(1-p)(1-q)M_B(0,0).\end{aligned} \tag{19}$$

The net magnetisation is also calculated as

$$M_{\mathrm{Net}} = |\langle M_A\rangle_c - \langle M_B\rangle_c|. \tag{20}$$

The total magnetic susceptibility of the system can be obtained by the following equation:

$$\chi = \chi_A + \chi_B \tag{21}$$

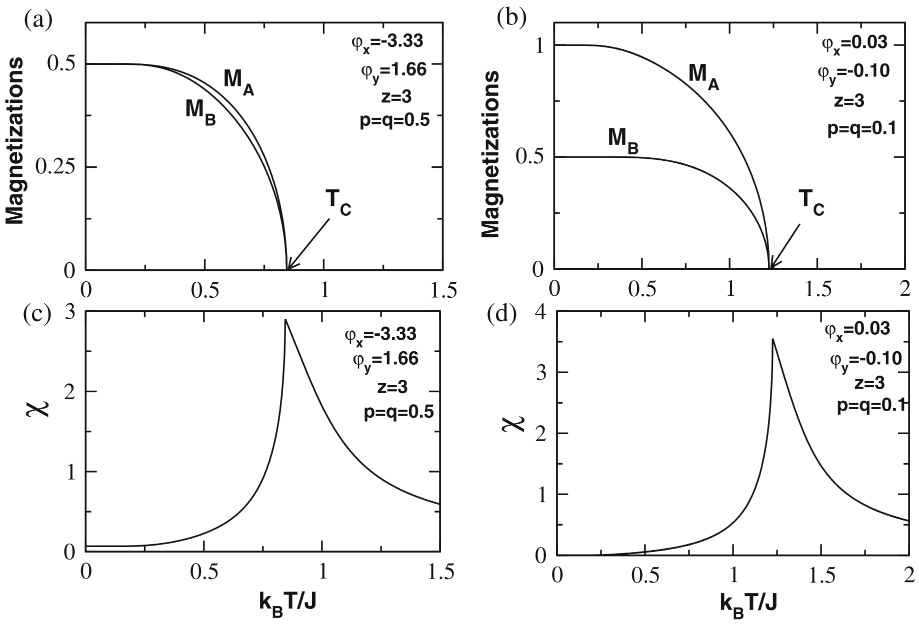

Figure 1. Behaviours of the order parameters, i.e. the sublattice magnetisations M_A and M_B and the total susceptibility χ as functions of the temperature for given values of model parameters as indicated in different panels.

where

$$\chi_A = \left(\frac{\partial \langle M_A \rangle_c}{\partial h}\right)_{h=0} \tag{22}$$

and

$$\chi_B = \left(\frac{\partial \langle M_B \rangle_c}{\partial h}\right)_{h=0}. \tag{23}$$

The pair of eq. (19) constitutes the necessary ingredient which is used to study the thermal behaviours of our model and to carry out the phase diagrams on various planes using an iterative procedure. In the next section, we present the numerical results of our calculations as illustrations.

3. Results and discussions

In this section, we present the results obtained by solving eqs (19)–(23) numerically. First, we have studied the thermal behaviours of the order parameters and compensation properties, then we have mapped the effects of RTSIA on the phase diagrams and finally the hysteresis properties of the model have been presented. All our calculations were only carried out for the coordination number $z = 3$.

3.1 *The thermal behaviours of order parameters and compensation properties*

Before starting this part, first we should give an explanation for the occurrence of compensation temperature. It should be noted that the compensation is favoured by two interactions acting in opposite directions. J aligns the spins of sublattice B in the z direction. For the given D_x and D_y values, the spins of sublattice A are oriented in a direction opposite to z. With the increase in the entropy of the system, the order is disturbed and at a given temperature, there is as much spin-up as there is spin-down and the magnetisations of the two sublattices are equal and non-zero at a specific temperature called the compensation temperature. At this temperature, M_A and M_B intersect as they are equal and so M_{net} is equal to zero. When the temperature is further increased, the thermal agitation overwhelms the magnetic interactions and the system loses magnetism at the transition temperature T_c.

The thermal variations of the sublattice magnetisations have been studied for given values of the model parameters in figures 1 and 2 to identify the available ground-state values, the compensation temperatures and the types of phase transitions which are also confirmed by the study of the thermal variations of the total magnetic susceptibility. Figures 1a and 1b indicate the existence of two ground-state values, i.e. 1/2 and 1, for sublattice magnetisation with

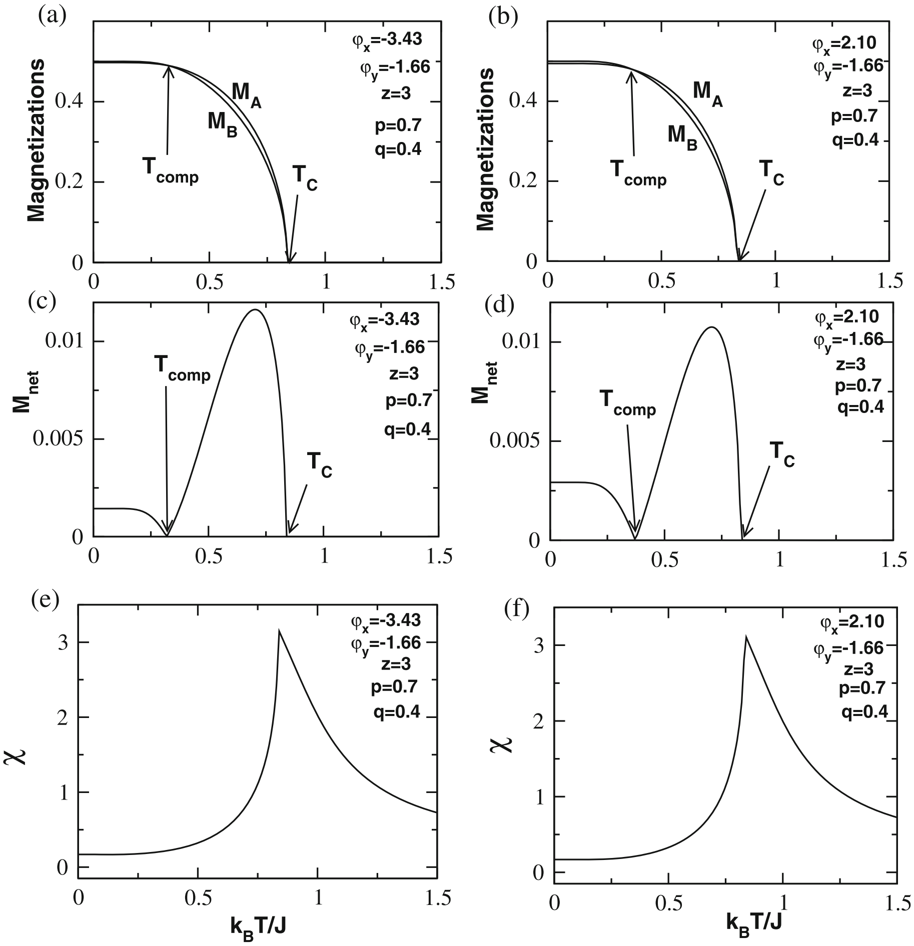

Figure 2. Behaviours of the order parameters, i.e. the sublattice magnetisations M_A and M_B, the net magnetisation M_{net} and the total susceptibility χ as functions of the temperature showing that the model exhibits the compensation behaviour for given values of the model parameters as indicated in different panels. T_c and T_{comp} indicate the second-order phase transition and the compensation temperatures, respectively.

spin-1 and only one ground-state value 1/2 for spin-1/2 as expected. M_A and M_B decrease continuously from their ground-state values with increasing temperature and finally vanish at the second-order phase transition temperature T_c where the magnetic susceptibility presents peaks as shown in figures 1c and 1d.

Figure 2 illustrates the existence of T_{comp} when $\varphi_y = -1.66$, for $\varphi_x = -3.43$, $p = 0.7$ and $q = 0.4$. Figures 2a and 2b show that M_A and M_B curves after starting from their ground-state values decrease as the temperature increases and then cross each other at T_{comp} before vanishing continuously at T_c. In figures 2c and 2d, we present the net magnetisation curves which first vanish at T_{comp} and then at T_c. Figures 2e and 2f show the thermal variations of magnetic susceptibilities which have the same behaviour as the previous figures. It should be noted that the compensation temperatures also exist for other values of our model parameters which will be presented later in detail in the phase diagram on the $(\varphi_x, k_BT/J)$ planes.

Figure 3 is obtained for various values of model parameters as indicated in different panels illustrated for the thermal variations of the net magnetisation. Five types, namely P-, Q-, R-, N- and L-types, of magnetisation behaviours as classified in the extended Néel nomenclature [32–34] are found.

In order to continue our investigation, we shall present the phase diagrams of the model on different planes of our variables in the next section.

3.2 *Thermal phase diagrams*

Before illustrating the phase diagrams on $(\varphi_x, k_BT/J)$ planes for $0 \leq p \leq 1$ and $0 \leq q \leq 1$, it should be noted that the $p = q = 1$ case corresponds to the pure Blume–Capel quantum model and the $p = q = 0$ case

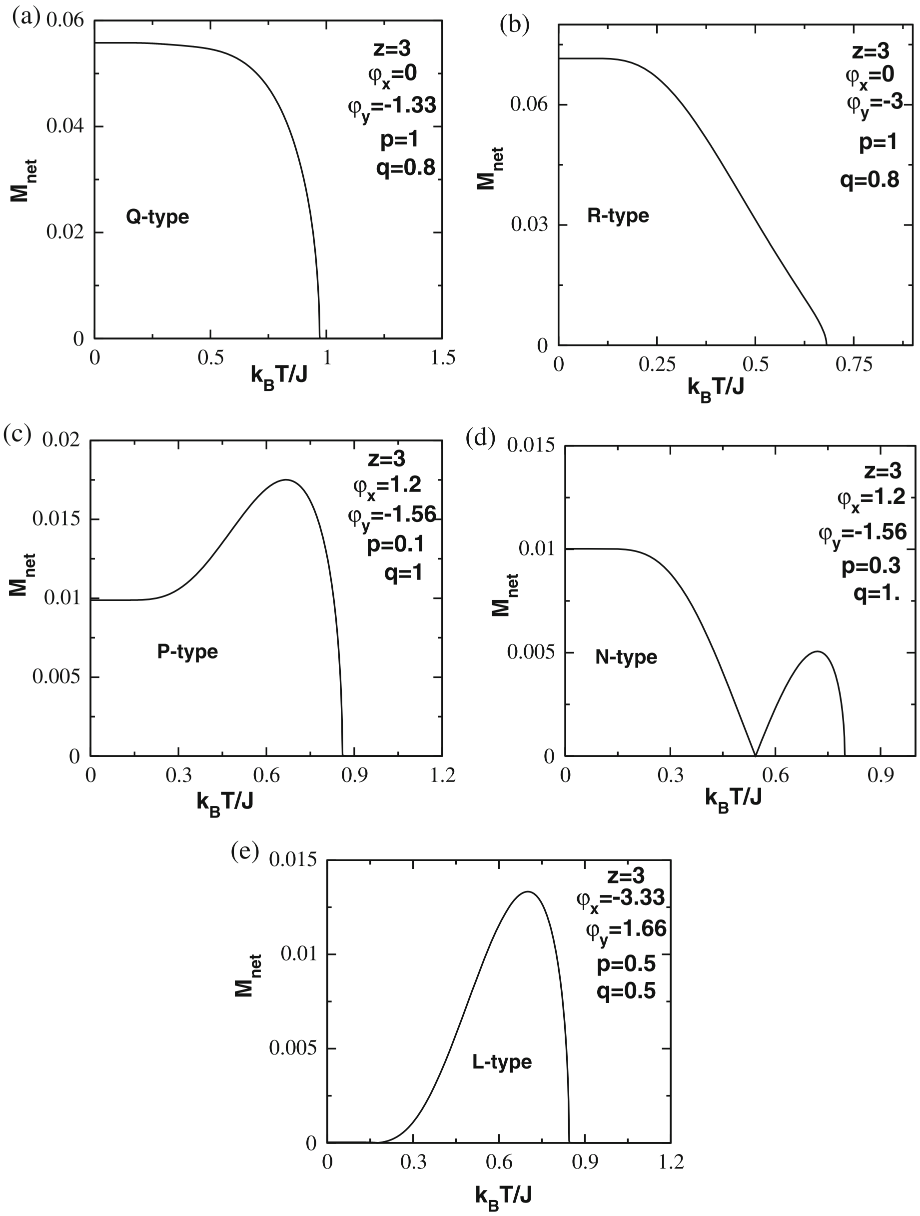

Figure 3. Thermal variations of the net magnetisation M_{net}. Values of model parameters are indicated in different panels. Different temperature dependencies of M_{net} are found to be of Q-, R-, P-, N- and L-types according to the extended Néel classification.

corresponds to the pure mixed spin-1 and spin-1/2 Ising model. This model becomes the random crystal field Blume-Capel quantum model when $0 < p < 1$ and $0 < q < 1$. The T_c and the T_{comp} lines are indicated with the solid and dotted lines, respectively in the phase diagrams.

The first phase diagrams, depicted in figure 4, are obtained at fixed values of q for $\varphi_y = -1.66$ by varying the values of p between 0 and 1 with the increments of 0.1. Figures 4a–4d show that for all values of q, the $p = 0.0$ lines are constant at T_c's which decrease with the increase of q. All the T_c-lines intersect at two points around $\varphi_x = 0$ at the temperature of $p = 0$ lines and these two points move away from each other as q increases. For $0.1 \leq q \leq 0.4$, the T_c-lines start from low temperatures for higher values of p when $\varphi_x < 0$ and they increase to the first intersection point where they remain constant until the second point from which they decrease to reach lower values of temperature for higher values of p when $\varphi_x > 0$. For $0.5 \leq q \leq 1$, the T_c-lines emerge at low temperatures as described above, then they increase, pass through the first intersection

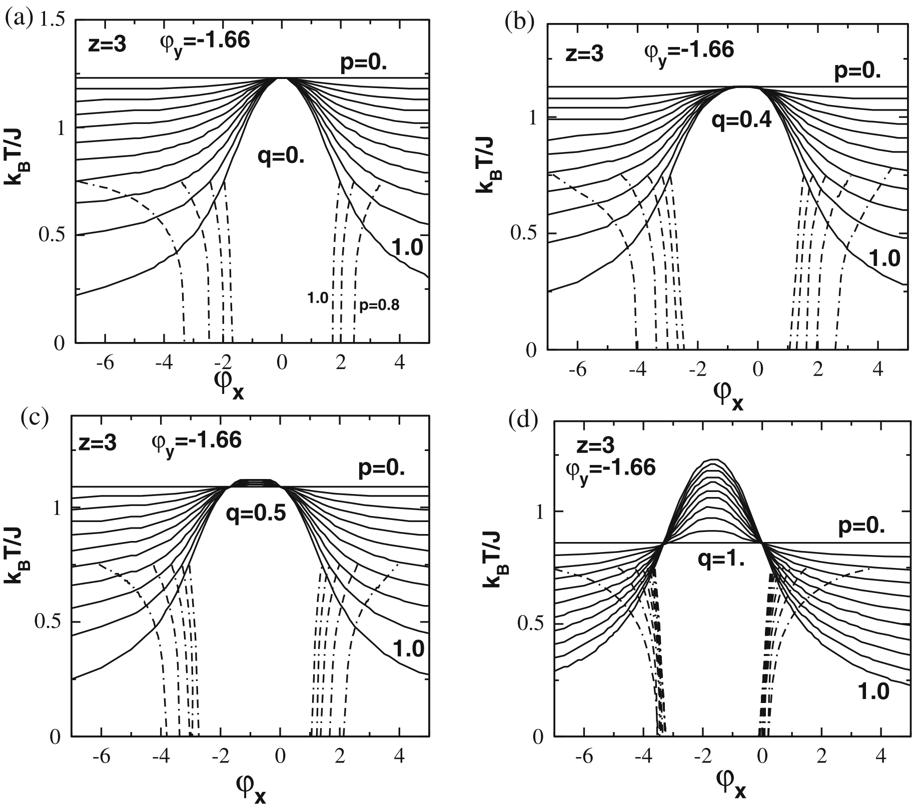

Figure 4. Phase diagrams displayed on the $(\varphi_x, k_\mathrm{B}T/J)$ planes for $\varphi_y = -1.66$ and given values of q and varying p with increment $\Delta p = 0.1$ as indicated in different panels: (**a**) $q = 0$, (**b**) $q = 0.4$, (**c**) $q = 0.5$ and (**d**) $q = 1$. The solid and dash–dotted lines indicate the second-order phase transition and compensation temperatures, respectively.

point and reach a peak from which they decrease passing through the second intersection point and tend towards lower temperatures. In figure 4a, the T_comp-lines are observed for $p = 0.8$–1.0 when $\varphi_x > 0.0$. They start from their corresponding T_c-lines and terminate at $k_\mathrm{B}T/J = 0.0$. When $\varphi_x < 0.0$, T_comp-lines are also observed for $p = 0.8$–1.0 in addition to $p = 0.7$ which was not observed when $\varphi_x > 0.0$. It should be noted that as p decreases, the T_comp-lines move to the left for $\varphi_x < 0.0$ and move to the right for $\varphi_x > 0.0$. They are all seen to be terminating at the same temperatures on their corresponding T_c-lines. Similar behaviours are also observed in figure 4b–4d. In figures 4b and 2c, calculated for $q = 0.4$ and 0.5, the T_comp-lines appear at $p = 0.6$ and are seen for $p =0.6$–1.0 in the regions with $\varphi_x > 0.0$ and $\varphi_x < 0.0$. Figure 4d which is obtained for $q = 1$ indicates the existence of T_comp-lines when $p \geq 0.2$. As seen, there are two T_comp-lines for each p. It is important to note that the φ_x range for which the T_comp-lines exist become large for the lower values of p.

The phase diagrams shown in figure 5 are realised for $\varphi_y = 1.66$ at fixed value of q by varying p. The T_c-lines are similar to those obtained in figure 4. For $q = 1$ as shown in figure 5d, no compensation line is observed for positive φ_x values. In fact, in figures 4 and 5, it is for all values of q that the T_c-lines intersect at two points located on either side of $\varphi_x = 0$. For lower values of q, the compensation only appears for higher values of p. This is explained by the fact that it is for higher p that a large number of sublattice A spins are influenced by the effect of D_y which forces them to be oriented in the opposite direction to that of sublattice B spins. The non-existence of T_comp for $\varphi_y = 0$ means that it is the interaction D_y which plays a preponderant role in the appearance of compensations. It facilitates the maintenance of spins in the opposite direction to z. For $\varphi_y < 0, \varphi_x < 0$ or $\varphi_y > 0, \varphi_x < 0$, the behaviour in terms of T_comp-lines is the same. For $\varphi_y < 0, \varphi_x > 0$ the number of T_comp-lines increases with q. But for $\varphi_y > 0$, $\varphi_x > 0$, this number remains constant until $q = 0.5$ before disappearing when $q = 1$. This means that the effects of $\varphi_x > 0$ is such that it reinforces the order in the sublattice A, that is to say that φ_x wins over φ_y by aligning a large number of spins in the same direction as the sublattice B spins.

We have presented the phase diagrams for $\varphi_y = 0$ in figure 6. The system is under the influence of only

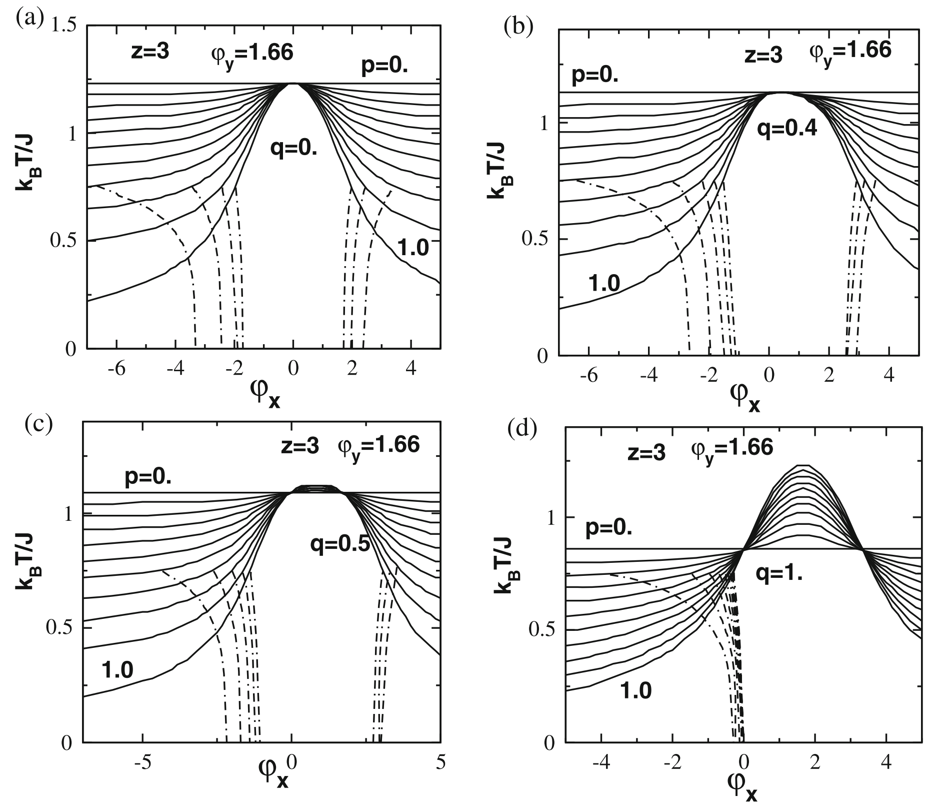

Figure 5. Phase diagrams displayed on the $(\varphi_x, k_\mathrm{B}T/J)$ planes for $\varphi_y = 1.66$ and given values of q and varying p with increment $\Delta p = 0.1$ as indicated in different panels: (**a**) $q = 0$, (**b**) $q = 0.4$, (**c**) $q = 0.5$ and (**d**) $q = 1$. The solid and dash–dotted lines indicate the second-order phase transition and compensation temperatures, respectively.

φ_x. The T_c-lines have similar behaviours. Whatever the values of p, there are no compensation lines. For $p = 1$, the model is turned into the mixed spin-1/2 and spin-1 Ising–Heisenberg models with zero longitudinal crystal field. The T_c-lines have similar trends with that obtained in figure 3b of [25] where the same model is investigated in the mean-field approximation.

Figure 7 obtained at fixed p values for $\varphi_y = -1.66$ and $0 \leq q \leq 1$ shows that all the phase transition lines are second-order. In figure 7a plotted for $p = 0$, all the T_c-lines are constant at their T_cs which decrease with increasing q. Figure 7b calculated for $p = 0.1$, reveals that the T_c-lines emerge from lower temperatures for higher qs when $\varphi_x < 0$ and then they increase with φ_x to reach a peak before $\varphi_x = 0$ and finally decrease to tend towards the lowest values of the temperatures. The peaks move further to the left of $\varphi_x = 0$ as q increases. The same behaviour is also observed on the phase diagrams of figures 7c–7f but with some additional properties. In figure 7c, obtained for $p = 0.4$, all the T_c-lines collapse closer to each other in the range of $-3.0 \leq \varphi_x \leq -1.0$. In figures 7d and 7e, calculated for $p = 0.5$ and 0.8 respectively, all the T_c-lines intersect at two points at different temperatures. Figure 7f indicates that for $p = 1$, these lines intersect only once. It should be noted that in these figures, the T_comp-lines appear to start from $p = 0.4$ for some q values with

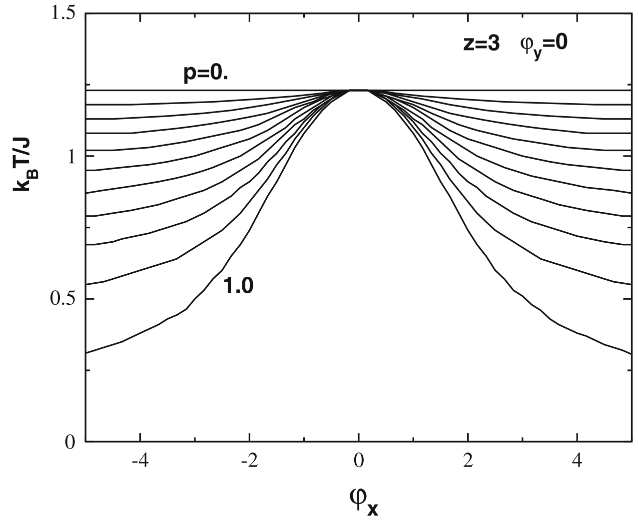

Figure 6. Phase diagrams displayed on the $(\varphi_x, k_\mathrm{B}T/J)$ planes for $\varphi_y = 0$ and varying p with increment $\Delta p = 0.1$ as indicated in different panels.

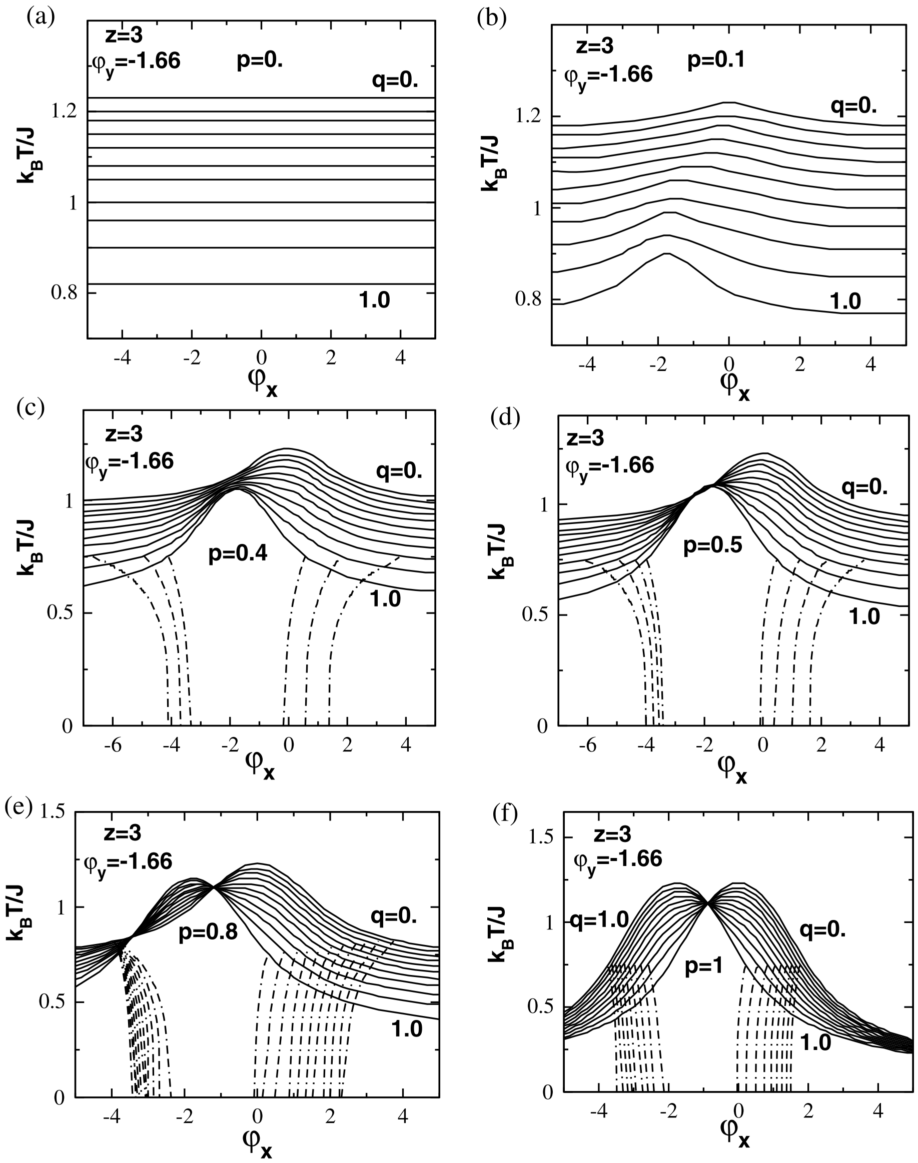

Figure 7. Phase diagrams displayed on the $(\varphi_x, k_BT/J)$ planes for $\varphi_y = -1.66$ and given values of p and varying q with increment $\Delta q = 0.1$ as indicated in different panels: (**a**) $p = 0$, (**b**) $p = 0.1$, (**c**) $p = 0.4$, (**d**) $p = 0.5$, (**e**) $p = 0.8$ and (**f**) $p = 1$. The solid and dash–dotted lines indicate the second-order phase transition and compensation temperatures, respectively.

two lines observed for the same q. When $p = 1$, the T_{comp}-lines are found for all q. The crossing of the T_c-lines of figures 7d–7f is realised for certain φ_x values. For these values, T_c remains the same for all q. This means that the entropy variation of the system from the ground state (where it is ordered) to transition (where it becomes disordered) remains constant. In other words, the energy to be supplied to the system so that it passes from the ferromagnetic phase to the paramagnetic phase does not vary whatever the number of sites of sublattice A subjected to the action of φ_x.

The last phase diagrams displayed in figure 8 are calculated on the $(p, k_BT/J)$ planes in figures 8a, 8c and 8e and on the $(q, k_BT/J)$ planes in figures 8b, 8d and 8f for $\varphi_y = -1.76$ for given values of φ_x. In figure 8a, we notice that for $\varphi_x = -1.66$ and $0 \leq q \leq 0.4$, the T_c-lines start from higher temperatures for lower values of q and decrease with p towards lower temperatures for lower values of q. The $q = 0.5$ lines are constant. For $0.6 \leq q \leq 1$, the T_c-lines start from lower temperatures for higher values of q and then increase with p towards higher temperatures for higher values of q. For $0 \leq q \leq 0.5$, the T_c-lines start from higher temperatures which decrease when q increase. Then, they decrease and tend towards low values of temperatures which increase with q. For $0.6 \leq q \leq 1$, the

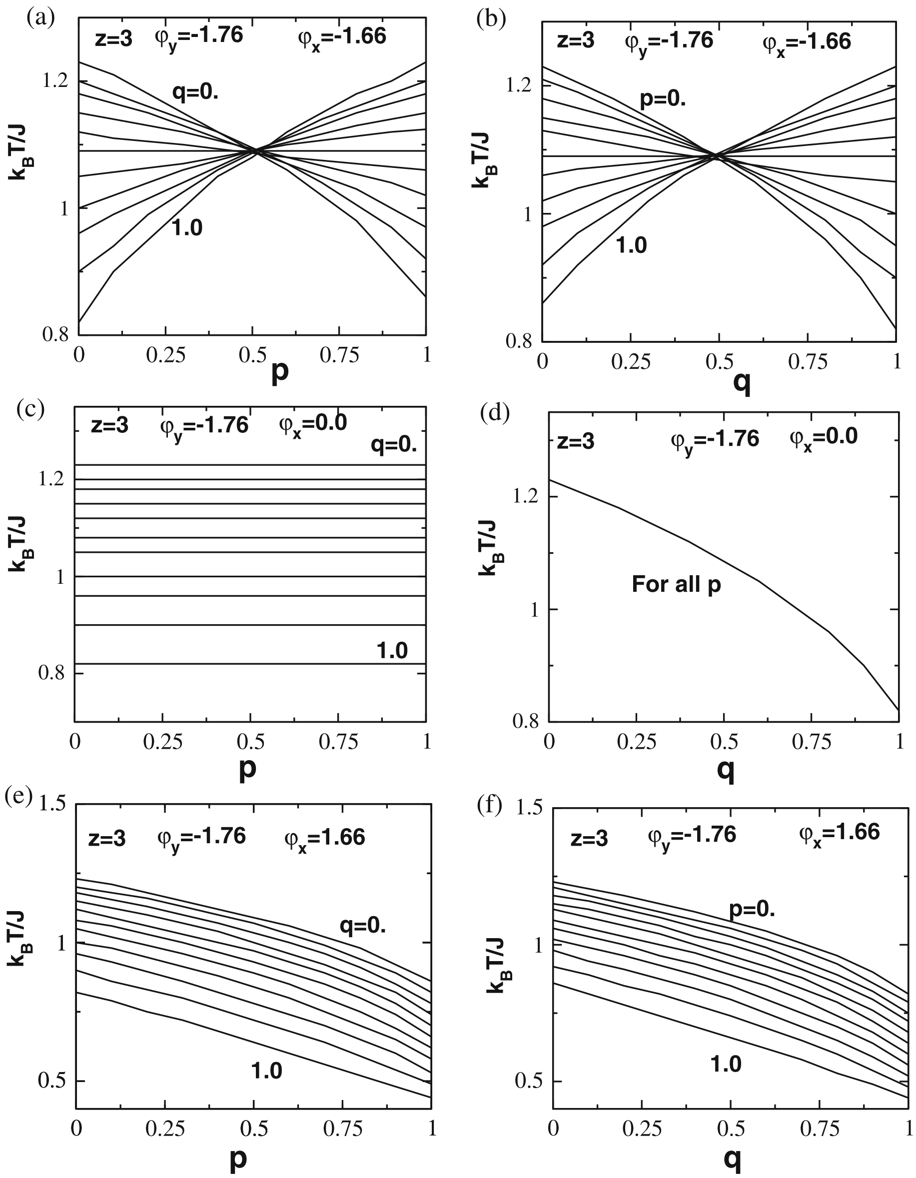

Figure 8. Phase diagrams displayed on the $(p, k_\mathrm{B}T/J)$ and $(q, k_\mathrm{B}T/J)$ planes for $\varphi_y = -1.76$ in the following cases: (**a**,**b**) $\varphi_x = -1.66$, (**c**,**d**) $\varphi_x = 0$, (**e**,**f**) $\varphi_x = 1.66$.

T_c-lines start from lower temperatures which decrease first with increasing values of q and at the second time, they increase and tend towards high values of temperatures which increase with q. All these lines intersect at $p = 0.5$ at the temperature of $q = 0.5$ line. Similar behaviours are also observed in figure 8b for the same values of φ_x. Figure 8c plotted for $\varphi_x = 0$ shows that the T_c-lines are constant at T_c which decrease with increasing q. These lines are combined together for all values of p and decrease when q increases as shown in figure 8d. Figure 8e calculated for $\varphi_x = 1.66$ indicates that the T_c-lines emerge from higher temperatures for lower values of q and decrease with p towards lower temperature for higher values of q. The behaviour obtained for the phase diagrams of figure 8f is similar to the one obtained in figure 8e.

3.3 *The hysteresis properties*

In the following, the hysteresis behaviours of our mixed spin system have been investigated for certain values of our model parameters. Figure 9 illustrates the influence of temperature on the hysteresis loops for $p = q = 0.5$ and $\varphi_y = -1.76$ for given values of φ_x. As can be seen, in figures 9a–9c realised for $\varphi_x = -1.66$, 0.0 and 1.66, respectively, the hysteresis loops get narrower as temperature increases and then they disappear at a temperature above the transition temperature.

In order to clarify the behaviour of the hysteresis loops with the variations of the system parameters, we have plotted in figure 10, the variations of the coercitive field H_c and the remanent magnetisation m_r as functions of the temperature and the RTSIA for $p = q = 0.5$. Figures 10a and 10b, calculated for $\varphi_x = 1.66$ and $\varphi_y = -1.76$, indicate that H_c and m_r decrease with the temperature. The variations of H_c and m_r as functions of φ_x are presented in figures 10c and 10d for $T = 0.15$ and $\varphi_y = -1.76$. We note the existence of two almost symmetric peaks of the same amplitude with respect to $\varphi_x = -1$. When $\varphi_x < -1.74$ and $-1 < \varphi_x < 0$, H_c and m_r increase with φ_x and reach their maximum values from which they respectively decrease for $-1.74 < \varphi_x < -1$ and $\varphi_x > 0$ towards their lowest values. In figures 10e and 10f, calculated for $T = 0.15$ and $\varphi_x = 0$, we have illustrated the variations of H_c and m_r as functions of φ_y. For negative/positive values of φ_x, values of H_c and m_r increase/decrease with φ_x and they present peaks at $\varphi_y = 0$.

Note that the narrowing of the hysteresis loops for $\varphi_x > 0$ implies a reduction in the coercive field H_c. Thus, for $\varphi_x > 0$ the intensity of the magnetic field required to reverse the spins decreases. Indeed, for $\varphi_x < 0$ the spins of sublattice A are oriented in the opposite direction to the spins of sublattice B while for $\varphi_x > 0$, all these spins are aligned in the same direction. It is therefore clear that the magnetic field necessary to reverse them (H_c) in the first case is large than that used in the second case. Hence, the narrowing of the hysteresis loop occurs in going from $\varphi_x > 0$ to $\varphi_x < 0$.

4. Conclusion

By employing the mean-field approximation based on the Bogoliubov inequality of the free energy, we have investigated the effects of RTSIA on the thermodynamic properties and phase diagrams of the mixed spin-1 and spin-1/2 Blume–Capel quantum model. The thermal behaviours of the sublattice magnetisations and the net magnetisation have been studied in detail and then the latter was classified according to the extended Néel nomenclature. The possible phase diagrams that we mapped for different values of the system parameters on the $(\varphi_x, k_B T/J)$, $(p, k_B T/J)$ and $(q, k_B T/J)$ planes present only the second-order phase transitions. This is interesting, as the mixed spin-1/2 and spin-1 Blume–Capel model also does not give any first-order phase transitions [35], i.e. the random crystal fields do not induce first-order transitions. The model yields one compensation temperature for certain values of system parameters and the possible compensation temperature lines are depicted on the $(\varphi_x, k_B T/J)$ planes. Under the effect of magnetic field, hysteresis loops are found

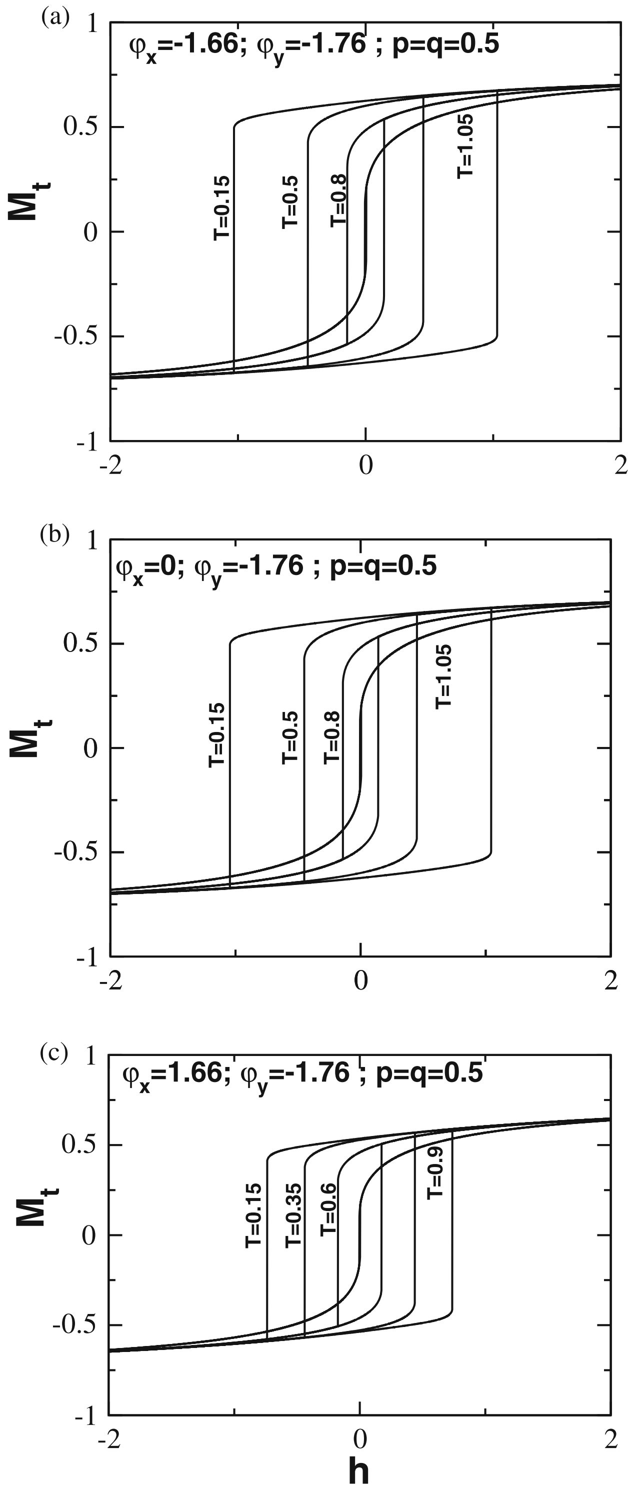

Figure 9. Total magnetisation M_t as a function of magnetic field h for several values of temperatures, for given model parameters $\varphi_y = -1.76$ and $p = q = 0.5$ in the following cases: (**a**) $\varphi_x = -1.66$, (**b**) $\varphi_x = 0$ and (**c**) $\varphi_x = 1.66$.

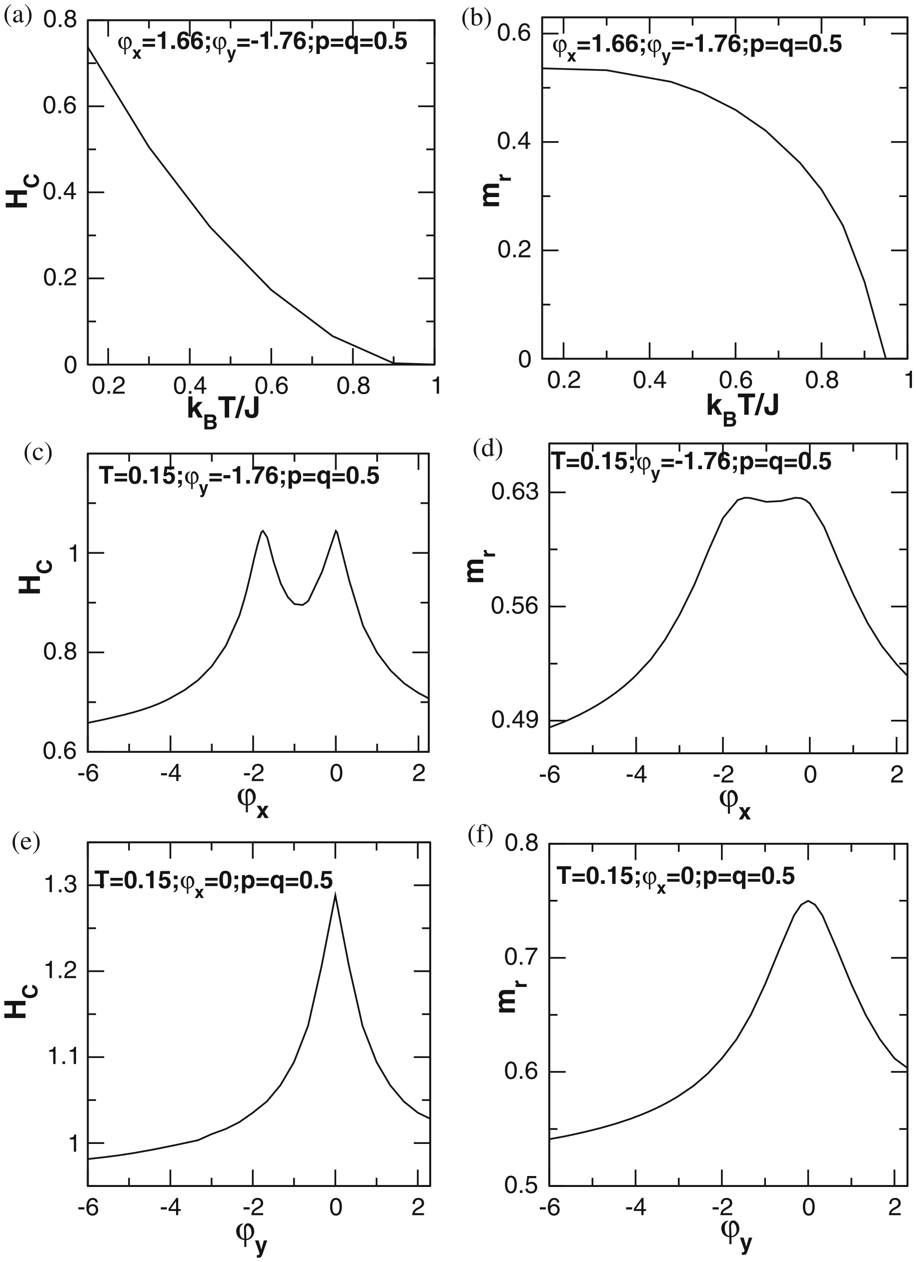

Figure 10. Coercive field H_c and remanent magnetisation m_r as functions of (**a**,**b**) the temperatures for $\varphi_y = -1.76$, $\varphi_x = 1.66$ and $p = q = 0.5$; (**c**,**d**) φ_x for $k_{\mathrm{B}}T/J = 0.15$, $\varphi_y = -1.76$ and $p = q = 0.5$; (**e**,**f**) φ_y for $k_{\mathrm{B}}T/J = 0.15$, $\varphi_x = 0$ and $p = q = 0.5$.

in the model and we have investigated their dependence on the temperature and the random single-ion anisotropies to specify the behaviours of the coercitive field H_c and the remanent magnetisation m_r. In the negative φ_x or φ_y range, H_c and m_r behaviours seem different from what we know in literature when the temperature varies. The compensation temperature and the hysteresis behaviours give possible usage of this system in science and technology. As far as we know, this is the first work which examines the effects of RTSIA on a mixed spin system. This means that no comparison of our results is therefore possible. We note that the model must be investigated for higher values of z so that the first-order phase transitions may also be observed and would be more interesting.

As a last word, we should note that the MFA is often used due to its simplicity as the first primary tool for the rough estimation of magnetic behaviour of spin systems.

The mixed spin-(1/2, 1) study including only D_x and D_y effects in BC model being the first, we can only compare it to exact calculation methods for certain values of the system parameters. Using exact methods, Strečka and Jaščur [21] studied the effect of uniaxial and biaxial crystal fields on the magnetic properties of mixed spin-(1/2, 1) Ising model on honeycomb lattice. The Hamiltonian describing this model is reduced to that used in our work when $D = 0$, $E = D_x$, $p = q = 1$ and $D_y = -D_x$. For $D_x > 0$ the T_c-line obtained in figure 4b is similar to the one we plotted in figure 4d. The difference is that T_c are different. For example, when $D_x = 4$, T_c is $\simeq$0.56 with our calculations whereas with the exact method it is $\simeq$0.22.

References

[1] S Ferlay, T Mallah, R Ouahès, P Veillet and M Verdaguer, *Nature* **378**, 701 (1995)
[2] D Gatteschi, O Kahn, J S Miller and F Palacio (eds.), *Magnetic molecular materials* (Kluver Academic Publishers, Dordrecht, 1991)
[3] O Kahn, *Molecular magnetism* (VCH, New York, 1993)
[4] J S Miller and M Drillon (eds.), *Magnetism: Molecules to materials V* (Wiley-VCH, Weinheim, 2005)
[5] R M White, *Science* **229**, 11 (1985)
[6] R Wood, *Understanding magnetism* (Tab Books Inc, Blue Ridge Summit, PA, 1988)
[7] E Köster, *J. Magn. Magn. Mater*. **120**, 1 (1993)
[8] L B Lueck and R G Gilson, *J. Magn. Magn. Mater*. **88**, 227 (1990)
[9] M Mansuripur, J. *Appl. Phys*. **61**, 1580 (1987)
[10] M Blume, *Phys. Rev*. **141**, 517 (1966)
[11] H W Capel, *Physica* **32**, 966 (1966)
[12] W Jiang, G B Xiao, G Z Wei, A Du and Q Zhang, *Commun. Theor. Phys*. **41**, 131 (2004)
[13] Y Belmamoun and M Kerouad, *Phys. Scr*. **77**, 025706 (2008)
[14] M Boughrara and M Kerouad, *Physica A* **374**, 669 (2007)
[15] K Htoutou, A Ainane and M Saber, *J. Magn. Magn. Mater*. **269**, 245 (2004)
[16] W Jiang, G Z Wei and A Du, *J. Magn. Magn. Mater*. **250**, 49 (2002)
[17] C Q Xu and S L Yan, *J. Magn. Magn. Mater*. **416**, 48 (2016)
[18] C Q Xu and S L Yan, *J. Magn. Magn. Mater*. **345**, 261 (2013)
[19] H Wu, G Wei, P Zhang, G Yi and W Gong, *J. Magn. Magn. Mater*. **322**, 3502 (2010)
[20] L čanová, J Strečka and T Lučivjanský, *Condens. Matter Phys*. **12**, 353 (2009)
[21] J Strečka and M Jašččur, *Phys. Rev. B* **70**, 014404 (2004)
[22] J Strečka and M Jašččur, *Physica A* **358**, 393 (2005)
[23] J Strečka and M Jašččur, *Condens. Matter Phys*. **8**, 869 (2005)
[24] W Jiang and G Z Wei, *Physica B* **250**, 236 (2005)
[25] E Albayrak, *Chin. Phys. Lett*. **35**, 037501 (2018)
[26] C M Salgado, N L de Carvalho, P H Z de Arruda, M Godoy, A S de Arruda, E Costabile and J R de Sousa, *Physica A* **522**, 18 (2019)
[27] I J Souza, M Godoy, A S de Arruda and T M Tunes, *Eur. Phys. J. B* **93**, 215 (2020)
[28] Y J Chen, S Hossain, L Miloslavsky, Y Liu, C Chien, Z P Shi, M S Miller and H C Tong, *IEEE Trans. Magn*. **36**, 3476 (2000)
[29] N X Sun and S X Wang, *IEEE Trans. Magn*. **36**, 2506 (2000)
[30] T Nozawa, N Nouchi and F Morimoto, *IEEE Trans. Magn*. **37**, 3033 (2001)
[31] H B Nie, C K Ong, J P Wang and Z W Li, *J. Appl. Phys*. **93**, 7252 (2003)
[32] M L Néel, *Ann. Phys*. **12**, 137 (1948)
[33] M Karimou, R A Yessoufou, A Kpadonou, T Oke and F Hontinfinde, *Condens. Matter Phys*. **19**, 33003 (2016)
[34] K M Hadey and F A Hasan, *J. Supercond. Nov. Magn*. **32**, 3971 (2019)
[35] E Albayrak and M Keskin, *J. Magn. Magn. Mater*. **261**, 203 (2003)